



Novel visible-light-driven AgX/graphite-like C₃N₄ (X = Br, I) hybrid materials with synergistic photocatalytic activity

Hui Xu^a, Jia Yan^a, Yuanguo Xu^a, Yanhua Song^a, Huaming Li^{a,*}, Jiexiang Xia^a, Chuanjing Huang^b, Huilin Wan^b

^a School of Chemistry and Chemical Engineering, School of the Environment, Jiangsu University, Zhenjiang 212013, PR China

^b State Key Laboratory Physical Chemistry of Solid Surfaces, Xiamen University, Xiamen 361005, PR China

ARTICLE INFO

Article history:

Received 16 May 2012

Received in revised form 27 July 2012

Accepted 14 August 2012

Available online 2 September 2012

Keywords:

g-C₃N₄

Silver halide

Graphite-like structure

Hybrid material

Photocatalytic

ABSTRACT

Novel visible-light-driven AgX/g-C₃N₄ (X = Br, I) hybrid materials were synthesized by the facile water bath method. The AgX/g-C₃N₄ hybrid materials were characterized by X-ray diffraction (XRD), energy dispersive X-ray spectrometer (EDS), transmission electron microscopy (TEM), X-ray photoelectron spectroscopy (XPS), UV–vis diffuse reflectance spectroscopy (DRS), photoluminescence (PL), Fourier transform infrared spectra (FTIR), Raman and the special surface area. The XRD, EDS, TEM, FTIR, Raman and XPS analyses indicated that AgX nanoparticles were evenly distributed on the surface of g-C₃N₄ and the heterostructures were formed. The photocatalytic activity of the AgX/g-C₃N₄ hybrid materials was evaluated using methyl orange as a target organic pollutant. The as-prepared AgX/g-C₃N₄ hybrid materials displayed much higher photocatalytic activity than the pure g-C₃N₄ and AgX nanoparticles. After the introduction of AgX nanoparticles, the photocurrent of the AgBr/g-C₃N₄ and AgI/g-C₃N₄ hybrid materials was found to increase by 21 and 8 times than that of the pure g-C₃N₄, respectively. The increased photocatalytic activity of the AgX/g-C₃N₄ hybrid materials was attributed to the synergic effect between g-C₃N₄ and AgX, which included the optical property, the better dispersion and the small size. A photocatalytic mechanism and the kinetics of AgX/g-C₃N₄ hybrid materials were also proposed.

© 2012 Elsevier B.V. All rights reserved.

1. Introduction

TiO₂, ZnO, WO₃ and other such kinds of materials have been widely used as the wide band gap semiconductor photocatalysts for clean energy and environmental protection [1–3]. In order to improve the limited optical absorption of the wide band gap semiconductor photocatalysts under the sunlight and to use sunlight source efficiently, a variety of visible-light-driven photocatalysts have been developed [4]. Two research paths have been pursued. One methodology is to extend the absorption spectrum of TiO₂ (or ZnO, WO₃, and so on) materials to the visible region, for example, via suitable textural design [5], modification by cation and/or anion doping [6], noble metal loading and forming semiconductor composites [7–10]. The other methodology is to develop novel sunlight-based photocatalysts, such as BiOX (X = Cl, Br, I) [11–13], BiVO₄ [14], and black titanium dioxide nanocrystals [15]. However, the developed visible-light-responsive photocatalysts are almost solely comprised of metal-based inorganic solids, and there is a

need to find a material that has appropriate band edge positions and adequate stability during the photocatalytic reaction.

Recently, graphite C₃N₄ (g-C₃N₄) material has attracted much attention in the field of photocatalysis for it is non-toxic and abundant [16]. Polymer-like semiconductor material (g-C₃N₄), only made up of carbon and nitrogen, can be used as a metal-free photocatalyst for solar energy conversion, hydrogen production and environment purification [17–21]. The metal-free polymeric photocatalyst can bring new prospects for solar energy and environment application, because the covalent g-C₃N₄ is a cheap, abundant and stable material with a controllable surface. Nevertheless, there are many drawbacks of the g-C₃N₄ material in the field of photocatalysis, which include: (1) the high recombination rate of photogenerated electron-hole pairs and low quantum efficiency, (2) lower specific surface area, and (3) the lack of absorption above 460 nm of g-C₃N₄ which requires additional techniques to utilize this range of irradiation in the photocatalytic reaction, for g-C₃N₄ has an optical band gap of 2.7 eV. Therefore, extending light absorption of g-C₃N₄ up to a large portion of the available solar energy becomes very necessary. To solve these problems, many methods have been proposed to improve the photocatalytic activity of g-C₃N₄ under visible light irradiation, and three strategies seem to be very efficient. Firstly, designing an appropriate g-C₃N₄

* Corresponding author. Tel.: +86 511 88791800; fax: +86 511 88791708.
E-mail address: lihm@ujs.edu.cn (H. Li).

textural structure helps to enhance the photocatalytic and adsorption ability. To make the carbon nitride polymer semiconductor more valuable for heterogeneous catalysis, the mesoporous carbon nitride polymer was prepared, which could function as a metal-free photocatalyst to activate O_2 for the selective oxidation of benzyl alcohols with visible light [22]. By utilizing the hard or soft template method, the morphological properties of $g\text{-C}_3\text{N}_4$ could be controlled to a certain extent, and finally the graphitic carbon nitride had a much bigger surface area [23–29]. Secondly, there is no denying that the chemical doping, including the anion or cation doping, is effective to extend the light responsive range and change the electronic structure of semiconductors as well as the surface properties, which helps to improve the photocatalytic activity. Various typical metals or metal oxide dopants have been studied [30–35]. The metal-containing carbon nitride compounds have been proved to be effective photochemical oxidation catalysts under visible light irradiation. It was found that $\text{Fe-g-C}_3\text{N}_4$ was active for the direct oxidation of benzene to phenol using the hydrogen peroxide [30]. The Fe and Cu metal components could strongly modify the electronic properties of $g\text{-C}_3\text{N}_4$ and provide the material with additional new functions [31,32]. Fe- and Cu-modified $g\text{-C}_3\text{N}_4$ was active for the hydroxylation of benzene to phenol using H_2O_2 [32]. The integration of Co_3O_4 nanoparticles within graphitic carbon nitride constructed a nanohybrid photocatalyst, achieving an apparent quantum efficiency of 1.1% at 420 nm for water to split to oxygen [33]. Compared with the pure $g\text{-C}_3\text{N}_4$ [34], the $\text{Ag/g-C}_3\text{N}_4$ photocatalysts exhibited significantly enhanced photocatalytic performance for the degradation of methyl orange and the hydrogen production. $\text{Pd@g-C}_3\text{N}_4$ was greatly active and promoted the selective formation of cyclohexanone [35]. In addition, non-metal doping $g\text{-C}_3\text{N}_4$ materials have also become attractive. Various non-metallic elements such as P [36], F [37], S [38,39], B [40,41] and graphene [42–44], were reported to have increased the catalytic activity of the $g\text{-C}_3\text{N}_4$ material under visible light illumination. Thirdly, coupling $g\text{-C}_3\text{N}_4$ with the other materials is also an effective method to raise the photocatalytic property of the pure $g\text{-C}_3\text{N}_4$, such as $\text{TiO}_2/\text{g-C}_3\text{N}_4$ [45,46], $\text{g-C}_3\text{N}_4/\text{TaON}$ [47], magnesium phthalocyanine ($\text{MgPc}/\text{g-C}_3\text{N}_4$) [48], $\text{g-C}_3\text{N}_4/\text{Bi}_2\text{WO}_6$ [49], $\text{ZnO/g-C}_3\text{N}_4$ [50], $\text{g-C}_3\text{N}_4/\text{SrTiO}_3$ [51], $\text{g-C}_3\text{N}_4/\text{SiO}_2\text{-HNb}_3\text{O}_8$ composites [52] and $\text{Fe}_3\text{O}_4/\text{g-C}_3\text{N}_4$ [53]. The introduction of functional elements or groups in the matrix or on the surface of $g\text{-C}_3\text{N}_4$ greatly improved its performance and extended applications. Therefore, the modification of $g\text{-C}_3\text{N}_4$ is very efficient to improve the optical absorption and photocatalytic performance under visible light irradiation. However, in the modification of $g\text{-C}_3\text{N}_4$ system, the light harvesting ability and quantum efficiency of the materials are still poor. So it is necessary to find appropriate compounds to further enhance the photocatalytic performance of $g\text{-C}_3\text{N}_4$.

Silver halide AgX ($X = \text{Br}, \text{I}$) is a very important photosensitive material extensively used in photography field. Its excellent photocatalytic property has also attracted wide attention [54–56]. Under visible light, the pure AgBr or AgI can absorb photons to generate electron–hole pairs. But the pure AgBr or AgI can be reduced to the $\text{Ag}^0\text{-AgBr}$ or $\text{Ag}^0\text{-AgI}$ structure. AgX can maintain its stability and photocatalytic activity if it is dispersed on certain support materials. It has been found that AgBr or AgI can maintain its stability and enhance the photocatalytic activity when AgX is coupled with TiO_2 [57–60], ZnO [61,62], WO_3 [63], Ag_3PO_4 [64], BiPO_4 [65], Fe_3O_4 nanoparticle [66,67], H_2WO_4 [68], MCM-41 [69,70] and zeolite [71]. Such supported AgX materials can display high photocatalytic activity and stability. There is one probable reason that the heterojunction structure is formed between AgX and the support materials. There are many literatures reporting that the heterojunction structure could significantly increase the photocatalytic activity [72,73]. Therefore, for AgX based composite photocatalysts, construction of composites with appropriate energy band and

heterojunction structure may obtain the high efficiency and stability. If $\text{AgX/g-C}_3\text{N}_4$ hybrid materials are prepared, it is likely that the graphite-like structure with higher photocatalytic performance can be obtained. To the best of our knowledge, there has been no report regarding the graphite-like type $\text{AgX/g-C}_3\text{N}_4$ hybrid materials or their application in the environment treatment field.

In this study, novel visible-light-driven $\text{AgX/g-C}_3\text{N}_4$ hybrid materials ($X = \text{Br}, \text{I}$) were synthesized by the facile water bath method. The photocatalytic activity of the $\text{AgX/g-C}_3\text{N}_4$ hybrid materials was evaluated using methyl orange (MO) as a target pollutant. The relationship between the photocatalytic activity and the structure property of $\text{AgX/g-C}_3\text{N}_4$ hybrid materials was discussed. A photocatalytic mechanism and the kinetics of $\text{AgX/g-C}_3\text{N}_4$ hybrid materials were also proposed.

2. Experimental

2.1. Preparation of photocatalysts

2.1.1. Preparation of graphitic carbon nitride

Graphitic carbon nitride ($g\text{-C}_3\text{N}_4$) was synthesized by directly heating dicyandiamide. Typically, 2 g of dicyandiamide powder was put into an alumina crucible with a cover, then heated at a rate of 2.9 K/min to reach a temperature of 350 °C, and then tempered at this temperature for another 2 h in a flowing-nitrogen atmosphere. It was followed by that the product was heated at a rate of 3.3 K/min to reach a temperature of 550 °C, and then tempered at this temperature for another 2 h in a flowing-nitrogen atmosphere.

2.1.2. Preparation of $\text{AgX/g-C}_3\text{N}_4$ hybrid materials

The $g\text{-C}_3\text{N}_4$ (0.1 g) as the substrate was added into 8 mL of ethylene glycol, and the suspension was sonicated for 20 min. Then, a certain quantity of 1-hexadecyl-3-methylimidazolium bromide ($[\text{C}_{16}\text{mim}]\text{Br}$) was added into the suspension, and the mixture was stirred magnetically for 30 min. Next, AgNO_3 , employed as the source of silver, was dissolved in the ammonia aqueous (25–28%) to obtain a $[\text{Ag}(\text{NH}_3)_2]^+$ solution. The $[\text{Ag}(\text{NH}_3)_2]^+$ and $[\text{C}_{16}\text{mim}]\text{Br}$ solution was quickly added to the $g\text{-C}_3\text{N}_4$ mixture, and the resulting suspensions were stirred at 90 °C in water bath for 6 h. According to this method, different molar ratios of the $\text{AgX/g-C}_3\text{N}_4$ ($X = \text{Br}, \text{I}$) samples were obtained and denoted as $\text{AgX/g-C}_3\text{N}_4(2.5\%)$, $\text{AgX/g-C}_3\text{N}_4(5\%)$, $\text{AgX/g-C}_3\text{N}_4(10\%)$, $\text{AgX/g-C}_3\text{N}_4(30\%)$ and $\text{AgX/g-C}_3\text{N}_4(50\%)$, respectively.

2.2. Characterization of photocatalysts

The crystalline phases of $\text{AgX/g-C}_3\text{N}_4$ hybrid materials were analyzed by X-ray diffraction (XRD) by Bruker D8 diffractometer with $\text{Cu K}\alpha$ radiation ($\lambda = 1.5418 \text{ \AA}$) in the range of $2\theta = 10\text{--}80^\circ$. The chemical composition of the samples was determined by X-ray energy dispersion spectrum (EDS). Transmission electron microscopy (TEM) micrographs were taken with a JEOL-JEM-2010 (JEOL, Japan) operated at 200 kV. Ultraviolet–visible (UV–vis) diffuse reflection spectra (DRS) were measured using a UV–vis spectrophotometer (Shimadzu UV-2450, Japan) in the range of 200–800 nm. BaSO_4 was used as the reflectance standard material. X-ray photoelectron spectroscopy (XPS) analysis was performed on an ESCALab MKII X-ray photo-electron spectrometer using the $\text{Mg K}\alpha$ radiation. The Fourier transform infrared spectra (FTIR) of the samples were recorded using Nicolet Nexus 470 spectrometer. Raman spectra were recorded at room temperature using a micro-Raman spectrometer (Renishaw Invia) in the backscattering geometry with a 532 nm laser as an excitation source. The nitrogen adsorption–desorption isotherms at 77 K were investigated using a TriStar II 3020 surface area and porosity analyzer (Micromeritics

Instrument Corporation, USA). The photoluminescence (PL) spectra of the samples were obtained by a QuantaMaster & TimeMaster Spectrofluorometer with an excitation wavelength at 325 nm.

2.3. Photocatalytic activity

Photocatalytic activity of the sample was evaluated by the degradation of MO under 300 W Xe lamp with a 400 nm cutoff filter. 0.075 g photocatalysts were added into 75 mL MO (10 mg/L) in a Pyrex photocatalytic reactor. Prior to irradiation, the suspensions were magnetically stirred for 30 min in the dark to ensure that the MO could reach the absorption–desorption equilibrium on the photocatalyst surface. Furthermore, all the experiments were performed at 30 °C under constant stirring. During every irradiation interval, 3 mL suspension was sampled and analyzed with a UV–vis spectrophotometer (UV-2450, Shimadzu) at the maximal absorption wavelength of MO, whose characteristic absorption peak was chosen to be 464 nm, and the concentration of 4-chlorophenol (4-CP) was also determined by an UV–vis spectrophotometer (UV-2450, Shimadzu) according to its absorbance at 225 nm.

2.4. Photoelectrochemical measurements

To investigate the transition of photogenerated electrons in AgX/g-C₃N₄ hybrid materials, g-C₃N₄ and AgX/g-C₃N₄ hybrid material electrodes were prepared. The photocurrents were measured with an electrochemical analyzer (CHI660B, Chen Hua Instruments, Shanghai, China) in a standard three-electrode system, which employed a platinum wire as counter electrode, a saturated calomel electrode (SCE) as reference electrode, and a GCE (3 mm in diameter) as working electrode, respectively. A 500-W Xe arc lamp was utilized as the light source. A 0.1 M Na₂SO₄ aqueous solution was used as the electrolyte. The modified electrode was prepared by a simple casting method as follows: 6 µL 2.0 mg/mL AgX/g-C₃N₄ aqueous solution was dropped onto the pretreated GCE and dried in air at room temperature to form AgX/g-C₃N₄ modified GCE (denoted as AgX/g-C₃N₄/GCE).

3. Results and discussion

3.1. Enhancement of photocatalytic activity

Fig. 1 shows the photocatalytic activity of AgBr/g-C₃N₄ and AgI/g-C₃N₄ materials with different content of AgX under visible light irradiation. In Fig. 1A and B, the blank test confirmed that MO could not be degraded within 10 min under visible light irradiation without catalysts, indicating that MO was a stable molecular and the photolysis could be ignored. In Fig. 1A, it was found that the pure g-C₃N₄ had low visible light photocatalytic activity, and the pure AgBr could degrade MO by 23% after 10 min under visible light irradiation. It was very interesting that when AgBr was combined with g-C₃N₄, the photocatalytic activity was increased to 91%. Compared with the pure AgBr, the photocatalytic degradation efficiency of MO by AgBr/g-C₃N₄ (30%) was enhanced about 70%. In Fig. 1B, it could be also seen that the photocatalytic efficiency of the pure g-C₃N₄ and AgI was much lower than that of AgI/g-C₃N₄ samples. After 3.5 h of visible light irradiation, the photocatalytic degradation efficiency of MO was about 28%, 44%, 79%, 81% and 62% for AgI/g-C₃N₄ (2.5%), AgI/g-C₃N₄ (5%), AgI/g-C₃N₄ (10%), AgI/g-C₃N₄ (30%) and AgI/g-C₃N₄ (50%), respectively. Moreover, 4-chlorophenol (4-CP) was chosen as another representative colorless model organic pollutant to further evaluate photocatalytic activity of AgX/g-C₃N₄ samples, as shown in Fig. 1C and D. After 6 h of irradiation, no degradation of 4-CP was observed in the direct photolysis, and only 6.1% of 4-CP was degraded over

bulk g-C₃N₄ under visible light irradiation. Fig. 1C and D indicates that photocatalytic activity of AgI/g-C₃N₄ and AgBr/g-C₃N₄ samples was much higher than that of the pure g-C₃N₄. It could be seen that 30% and 53% of 4-CP was degraded in the case of AgBr/g-C₃N₄ and AgI/g-C₃N₄ samples, respectively, indicating that the AgX/g-C₃N₄ materials were efficient visible-light-driven photocatalysts.

Therefore, it was interesting to indicate that the formation of the AgX/g-C₃N₄ structure greatly enhanced the photocatalytic activity. In the experiment, it was important to note that the mechanical blend did not obviously enhance the photocatalytic activity of AgX and g-C₃N₄, implying that there may be some interaction between g-C₃N₄ and AgX, which played an important role in increasing the photocatalytic activity. The mechanism of improving photocatalytic activity was expected to be investigated, that is to say, the reason behind the phenomenon – the improvement of photocatalytic activity – was worth studying.

The variation of UV–vis absorption spectra of MO degradation using g-C₃N₄ and AgX/g-C₃N₄ materials is shown in Fig. 2. Under visible light illumination, with AgBr/g-C₃N₄ materials, the color of MO solution changed from yellow to light yellow and then disappeared during the reaction. The peak intensity of the UV–vis absorption related to MO decreased sharply, and the main absorption band at 464 nm almost completely disappeared after 20 min, which indicated the chromophoric structure of the MO dye was decomposed. On the contrary, the variation of absorption spectra of MO degradation using g-C₃N₄ as the photocatalyst was slight. The effect of pH on the degradation of MO was also tested, and the results are shown in Fig. S1.

It was worth pointing out that the stability of the photocatalyst was crucial for the practical application. The stability test of the AgX/g-C₃N₄ hybrid materials was conducted by performing the MO bleaching reactions repeatedly for five times, as shown in Fig. S2. The photocatalytic efficiency decreased slightly after five times due to the loss of catalyst in the recycling process, and the catalyst exhibited high activity after five successive cycles under the visible light irradiation. These results indicated that AgX/g-C₃N₄ hybrid materials remained effective and reusable.

3.2. Kinetics

To investigate the kinetics of MO degradation by the AgX/g-C₃N₄ samples, a pseudo-first-order reaction model was applied to describe the experimental data as follows:

$$-\ln \left(\frac{C}{C_0} \right) = k_{ap}t$$

where k_{ap} is the apparent reaction rate constant, C_0 is the adsorption equilibrium concentration of MO, t is the reaction time, and C is the concentration of MO at the reaction time t . In Fig. 3, it was found that all of the AgX/g-C₃N₄ photocatalysts exhibited higher photocatalytic degradation rate than the pure g-C₃N₄ sample under visible light irradiation. The photocatalytic degradation rate was enhanced gradually with the increasing content of AgX. The apparent rate constant k of AgBr/g-C₃N₄ (30%) and AgI/g-C₃N₄ (30%) was 0.19 min^{−1} and 0.41 h^{−1}, respectively, which was 39.0 times and 12.1 times as high as that of the pure g-C₃N₄. At the same time, the k of AgBr/g-C₃N₄ (30%) and AgI/g-C₃N₄ (30%) was 10.9 times and 12.8 times higher than that of the pure AgBr and AgI, respectively. It could also be seen from the insert graph of Fig. 3 that the content of AgX had a great influence on the photocatalytic activity of the prepared materials.

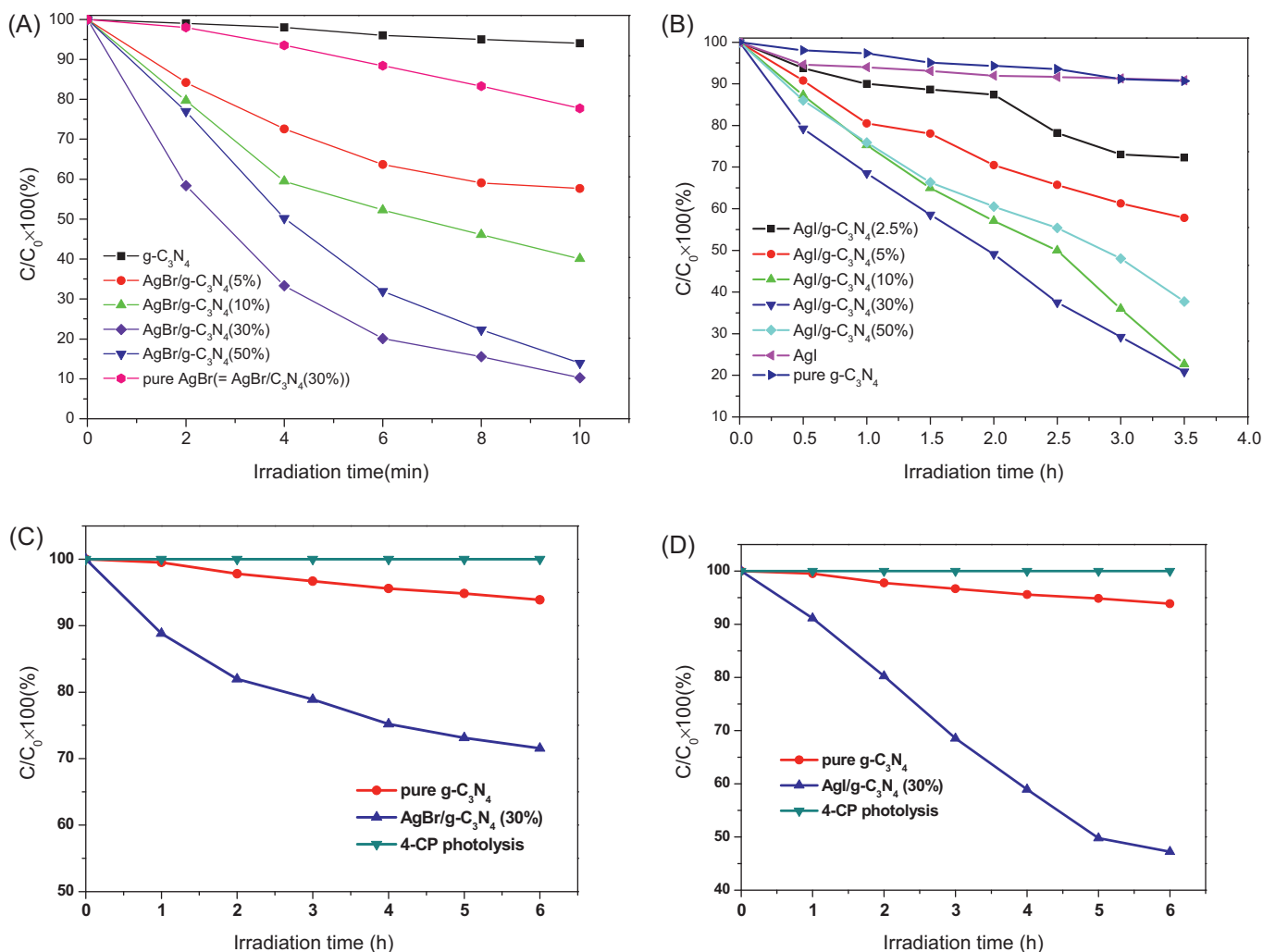


Fig. 1. Photocatalytic degradation of MO by (A) AgBr/g-C₃N₄ and (B) AgI/g-C₃N₄ structures under visible light irradiation, and time course of 4-CP conversion on AgBr/g-C₃N₄ (C) and AgI/g-C₃N₄ samples (D).

3.3. Structure and morphology characterization of AgX/g-C₃N₄ photocatalysts

The XRD patterns of the as-prepared AgX/g-C₃N₄ composites with different AgX content are shown in Fig. 4. The characteristic peak of g-C₃N₄ around 27.4° could be clearly identified because of the pure g-C₃N₄ sample, which was indexed as (002) diffraction plane (marked with “♦”). The XRD peak at 27.4° in g-C₃N₄ was due to the stacking of the conjugated aromatic system [18,31]. With the increasing AgBr content (Fig. 4A), the diffraction peaks at 26.8°, 31.0°, 44.4°, 52.6°, 55.1°, 64.6° and 73.3° gradually appeared and the intensity increased, and the peaks were assigned to the (111), (200), (220), (311), (222), (400) and (420) planes of AgBr crystal (JCPDS file: 6-438), respectively [56]. In Fig. 4B, the peaks at $2\theta = 22.3^\circ, 23.7^\circ, 25.3^\circ, 32.8^\circ, 39.2^\circ, 42.6^\circ$ and 45.6° were indexed to (100), (002), (101), (102), (110), (103) and (112) planes of the hexagonal β -AgI crystal phase (JCPDS file: 09-0374), respectively [74]. However, no typical patterns of g-C₃N₄ (002) were observed in AgX/g-C₃N₄ composites with the high AgX content (>50%), which was due to the low g-C₃N₄ content in the samples. Therefore, in the XRD analysis, no impurity peaks were observed, which confirmed the high purity of the AgX and C₃N₄ products.

Fig. 5 shows a comparison of the FTIR spectra of the pure g-C₃N₄ and AgX/g-C₃N₄ composites. In the case of pure g-C₃N₄, the strong bands in the 1200–1650 cm⁻¹ region were found in the spectrum,

with the peaks at 1242, 1322, 1412, 1563, and 1634 cm⁻¹, which corresponded to the typical stretching vibration modes of C=N and C–N heterocycles [42,50]. Additionally, the characteristic breathing mode of triazine units at 807 cm⁻¹ was observed [42,50]. It could also be clearly seen that the main characteristic peaks of g-C₃N₄ appeared in all AgX/g-C₃N₄ photocatalysts. In the case of the AgX/g-C₃N₄ composites, the characteristic peaks of g-C₃N₄ did not move (red shift or blue shift) after the introduction of AgX nanoparticles. This result indicated that in the AgX/g-C₃N₄ system, there was no covalent bond between g-C₃N₄ and AgX nanoparticles, which was different from the ZnO/C₃N₄ materials [50]. The AgX nanoparticles might be deposited and well dispersed on the g-C₃N₄ surface, and the EDS, TEM characterization would be analyzed in detail.

The Raman spectra of the samples are shown in Fig. S3. In the g-C₃N₄ sample, the weak characteristic peaks of g-C₃N₄ at 458, 693 and 734 cm⁻¹ were observed [42]. In the case of the AgBr/g-C₃N₄ and AgI/g-C₃N₄ photocatalysts, a relatively strong and clear Raman vibration at 484 cm⁻¹ was observed, which could be due to the presence of AgX.

The detailed structural information about the AgX/g-C₃N₄ composites was further investigated by TEM (Figs. 6 and S4). From the TEM pictures in Fig. 6A and B, the smooth and flat layers in the pure g-C₃N₄ sample could be clearly seen, which was consistent with the reported results [18,51]. The crystalline structure had been confirmed by the XRD data (Fig. 4). Fig. 6C and D shows

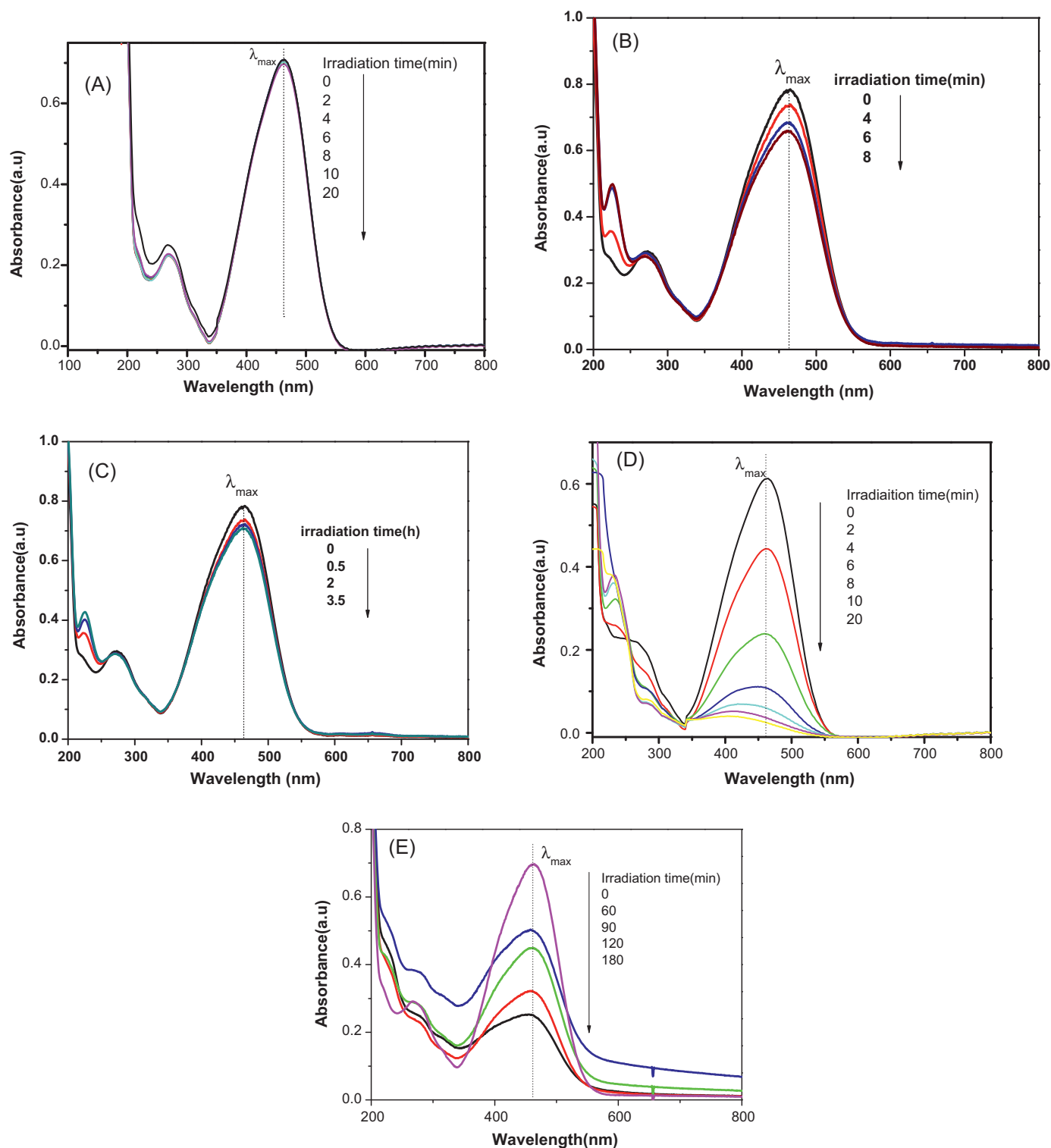


Fig. 2. Temporal absorption spectral patterns of MO dye during the photodegradation process by g-C₃N₄ (A), AgBr (B), AgI (C), AgBr/g-C₃N₄ (D) and AgI/g-C₃N₄ (E) sample.

typical TEM images of the representative AgBr/g-C₃N₄ (10%) and AgBr/g-C₃N₄ (30%), and Fig. 6E and F shows typical TEM images of the representative AgI/g-C₃N₄ hybrid material (10% and 30%). It was obvious that the diameters of AgX nanoparticles were in the range of 8–12 nm and the average diameter of AgX nanoparticles was about 10 nm. The TEM images of the AgBr/g-C₃N₄ hybrid materials (2.5%, 5%, 50%), AgI/g-C₃N₄ composites (2.5%, 5%, 50%), pure AgBr and pure AgI are shown in Fig. S4. The AgX nanocrystals anchoring on the surface of g-C₃N₄ looked like rivet and had a

good dispersion behavior on the layered material, which could offer more photocatalytic reaction centers. Therefore, it was expected to offer an increased photocatalytic activity. The interaction between the AgX nanoparticles and the g-C₃N₄ layered materials was so strong that ultrasonication during the sample preparation procedure for TEM analysis could not peel off these nanoparticles. The AgX nanoparticles were dispersed on the surface of g-C₃N₄ and a heterojunction structure was formed. The EDS pattern (Fig. S5) indicated the AgX/g-C₃N₄ composites contained C, N, Ag, and X (X = Br,

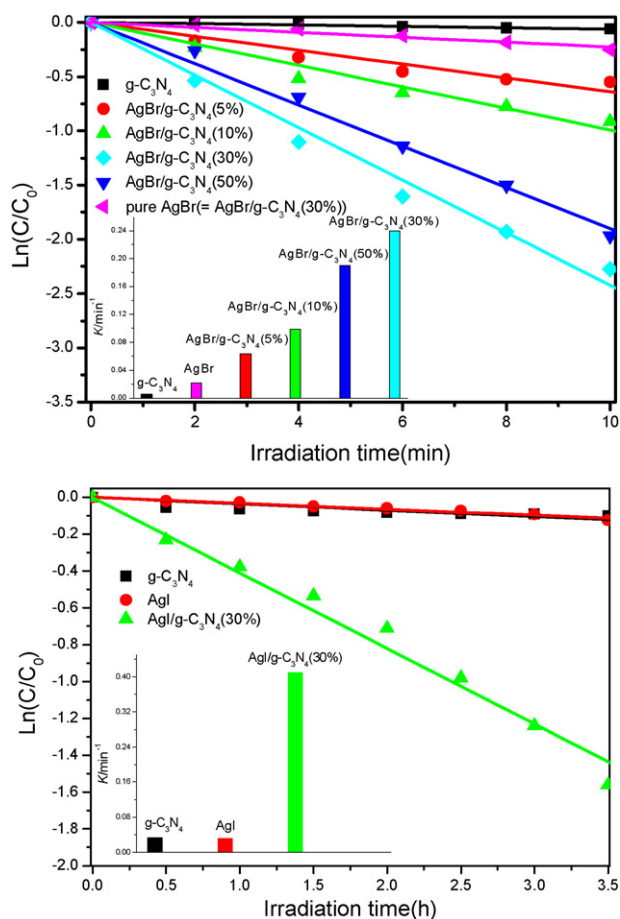


Fig. 3. Photocatalytic degradation kinetics of MO over AgX/g-C₃N₄ (X = Br, I) composites under visible light irradiation.

I) element, and the Si element was attributable to the Si foil. The results of gravimetric method analysis are listed in Table S1. The results indicated that the experimental value of the AgX contents was lower than the theoretical value.

Fig. S6 shows the XPS spectra of the pure g-C₃N₄ and AgX/g-C₃N₄ hybrid materials. The survey scan XPS spectrum showed that the g-C₃N₄ and AgX/g-C₃N₄ samples all contained carbon, nitrogen and a small amount of oxygen. The oxygen might be absorbed from the atmosphere during the survey scan. In the case of the AgBr/g-C₃N₄ sample, the strong peaks of Ag 3d, Ag 3p, Br 3d, Br 3p, C 1s, N 1s and O 1s were observed in the XPS spectra. The XPS spectra also demonstrated the presence of Ag and I species in the AgI/g-C₃N₄ sample, which corresponded to Ag 3d, Ag 3p, I 3d, I 3p and I 4d.

The typical high resolution XPS spectra are shown in Fig. 7. As can be seen from Fig. 7A, C 1s spectrum could be deconvoluted into two peaks, and all samples had the C peak at 284.6 eV and 288.1 eV, which could be ascribed to carbon and defect-containing sp²-bonded carbon (C=N) [34,42]. This result was in good agreement with the literature [34,42]. Fig. 7B shows the high-resolution N 1s XPS spectra of the samples. The main N 1s peak at a binding energy of 398.6 eV could be attributed to sp²-hybridized nitrogen (C=N–C) [42]. The high resolution XPS spectra of Ag 3d in the AgX/g-C₃N₄ hybrid materials are shown in Fig. 7C. It showed that the peaks of Ag 3d located at about 367.8 eV and 373.8 eV, which could be attributed to the Ag 3d5/2 and Ag 3d3/2 binding energies, respectively. In particular, the peaks at 367.9 eV and 373.9 eV were ascribed to Ag⁺ of the AgBr or AgI material [58,75]. Such similar results have been reported by other researchers [58,75]. The Br 3d spectra in AgBr/g-C₃N₄, are shown as in Fig. 7D. The peak at 68.4 eV

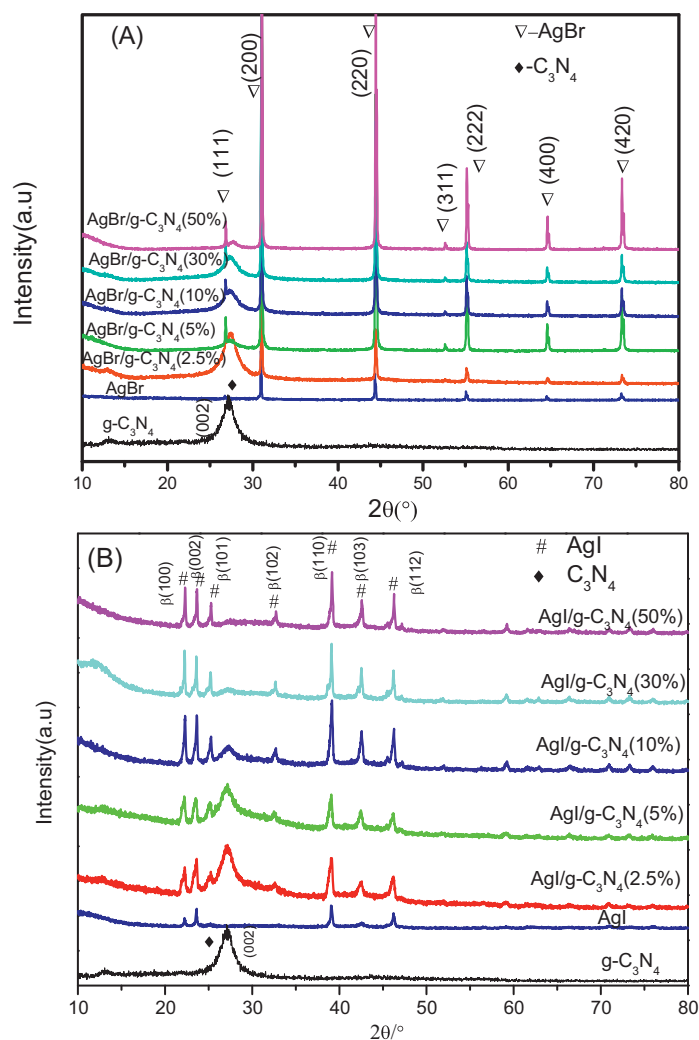


Fig. 4. X-ray diffraction patterns of (A) AgBr/g-C₃N₄ and (B) AgI/g-C₃N₄ composites.

was attributed to Br 3d. Fig. 7E shows XPS spectra of I 3d in the AgBr/g-C₃N₄ composite. The I 3d XPS peaks could be resolved into two typical peaks, of which 620.0 eV and 631.4 eV were ascribed to binding energies of I 3d3/2 and I 3d5/2, respectively, which was in good agreement with those in AgI [76]. Based on the XPS analysis, the Ag⁺ and bromide ions were on the surface of g-C₃N₄ in the AgX/g-C₃N₄ hybrid materials. All of these results further confirmed the coexistence of AgX and g-C₃N₄ in the AgX/g-C₃N₄ heterostructures.

The DRS spectra of the pure g-C₃N₄ and AgX/g-C₃N₄ hybrid materials are shown in Fig. 8. The band gap of the pure g-C₃N₄ was estimated to be 2.7 eV, which corresponded to wavelengths shorter than 460 nm. This result was in agreement with the previous reports [16]. Upon the AgX nanoparticles deposited on the surfaces of g-C₃N₄ layer, the absorption edge of heterocrystals was extended to around 480 nm. The absorption intensity of the AgX/g-C₃N₄ hybrid materials was slightly strengthened with the increasing AgX content. It was noted that the AgX/g-C₃N₄ samples also exhibited a broad background absorption in the visible light region. This could be attributed to the presence of AgX nanoparticles in the AgX/g-C₃N₄ hybrid materials. The AgX/g-C₃N₄ samples showed stronger broad background absorption with the increasing AgX content, which was in accordance with the color changing from yellow to gray. The enhanced light absorption of the AgX/g-C₃N₄ hybrid materials led to the production of more electron–hole pairs

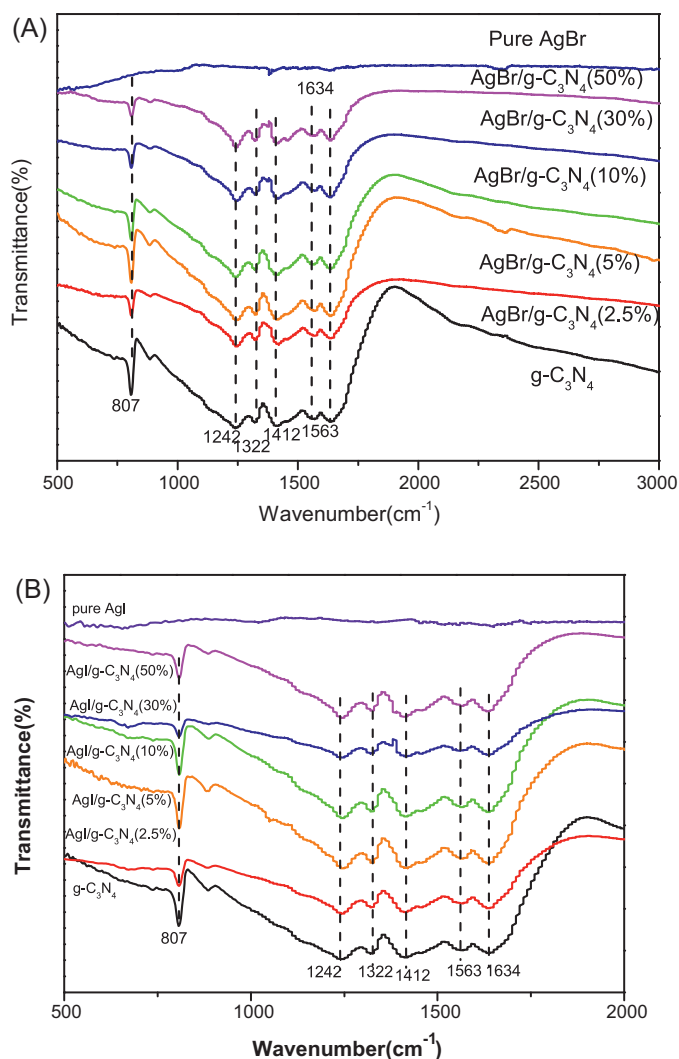


Fig. 5. FTIR spectra of (A) AgBr/g-C₃N₄ and (B) AgI/g-C₃N₄ samples.

under the visible light irradiation, which subsequently resulted in a higher photocatalytic activity.

3.4. Structure–activity relationships and the mechanism of enhancement of photoactivity

In the photocatalytic activity analysis of the samples, it was confirmed that the AgX/g-C₃N₄ could significantly enhance the photocatalytic degradation efficiency. It was necessary to elaborate the reasons for the increased photocatalytic activity. Therefore, it was necessary to study the structure and morphology characterization of AgX/g-C₃N₄ photocatalysts. The photocatalytic degradation experiment showed the photocatalytic performance of the material, and that was “what the photocatalytic performance is”. The material characterization analysis was to explain the structure and the composition of the photocatalyst, and that was “what the structure of the materials is”. The aim of this work was to explain why the structure would have photocatalytic performance.

In the photocatalytic ability analysis, it could be seen that the photocatalytic activity of the AgBr/g-C₃N₄ (30%) and AgI/g-C₃N₄ (30%) hybrid composites was essentially higher than that of the corresponding pure AgBr and AgI nanospecies (by a factor of ca. 10.9 and 12.8, respectively, in Fig. 3). In Fig. 1A and B, when AgX load amounts to more than 30%, the photocatalytic activity decreased with the increasing AgX amount. The optimal AgX loading content

on the surface of the g-C₃N₄ to achieve an improved photocatalytic activity was determined to be 30%. The reason why excessive AgX content decreased the photocatalytic degradation efficiency of the AgX/g-C₃N₄ hybrid materials could be concluded as follows: a large amount of AgX on the surface of g-C₃N₄ resulted in the agglomeration of AgX particles, which is shown in Fig. S4 C and F. The TEM image of the large AgX content on the g-C₃N₄ surface (50%) indicated an average particle size was about 100 nm, which was larger than that with the 10% and 30% AgX loading samples (Fig. 6). This result was attributed to AgX nanoparticles agglomerating. The high AgX content could significantly affect the size and the dispersion. Many literatures reported that the size and the dispersion of nanoparticles on the surface of the semiconductors could affect the catalytic activity [77]. In the Ag/ZnO system, the photocatalytic activity of Ag/ZnO photocatalysts mainly depended on the dispersity of metallic Ag in Ag/ZnO Nanocatalyst [78]. Therefore, the smaller the size was and the higher the dispersion of AgX on the surface of the g-C₃N₄ was, the higher the photocatalytic activity of AgX/g-C₃N₄ hybrid materials should be. At the same time, the larger AgX nanoparticle size could weaken the anchored force between the substrate and AgX, which could destruct the heterojunction structure [79]. So the photo-excited electron and hole separation efficiency was low, which could result in the decrease of photocatalytic activity of the higher AgX content loading samples. Therefore, only AgX nanoparticles with an appropriate size and dispersion were effective for the enhancement of the photocatalytic activity of g-C₃N₄. It was also found that AgBr/g-C₃N₄ had higher photocatalytic activity than the AgI/g-C₃N₄ hybrid composites with the same AgX content, as illustrated in Fig. 9.

The photocatalytic activity of catalysts depended on many factors, such as crystallinity, surface property, morphology, optical property, and size. The different photocatalytic activity of the samples could be elaborated by the following aspects.

It was reported that the effect of the large BET specific surface area was beneficial to the increase of the photocatalytic activity of the composites. All the AgBr/g-C₃N₄ hybrid materials had similar surface areas with the pure g-C₃N₄, which is shown in Table S2. It was indicated that the surface area was not the main factor to enhance the photocatalytic performance. Optical property was also important for the high activity of hybrid materials. The AgX/g-C₃N₄ hybrid materials showed an intense, broad background absorption in the visible light region, as shown in Fig. 8. This result indicated that the hybrid samples could absorb more photons, which was favorable for the photocatalytic reaction. Many literatures confirmed that the size effect of nano-size materials could be considered as an important factor to increase the photocatalytic activity [80]. The high photocatalytic behavior of AgX/g-C₃N₄ hybrid materials might also be assigned to a better dispersion and a small size of AgX on the g-C₃N₄ surface. However, once the deposition content was increased, negative effect appeared. The decrease of photocatalytic activity for higher AgX loading was directly connected to the merging of AgX agglomerates. According to the above analysis, the increasing photocatalytic activity of the AgX/g-C₃N₄ hybrid materials was attributed to the synergic effect between g-C₃N₄ and AgX, which could efficiently separate the electron and hole pairs.

In order to investigate the influence of the AgX, photoluminescence spectra analysis was applied to investigate the separation efficiency of photogenerated electrons and holes in AgX/g-C₃N₄ samples. Fig. 10 shows the PL spectra of the pure g-C₃N₄ and AgX/g-C₃N₄ hybrid materials excited by 325 nm. It could be found that the main emission peak was centered at about 460 nm for the pure g-C₃N₄ sample, which was similar to the literatures [81]. For AgX/g-C₃N₄ hybrid materials, the position of the emission peak in the PL spectrum was similar to that of the pure g-C₃N₄, but the emission intensity significantly decreased, which indicated

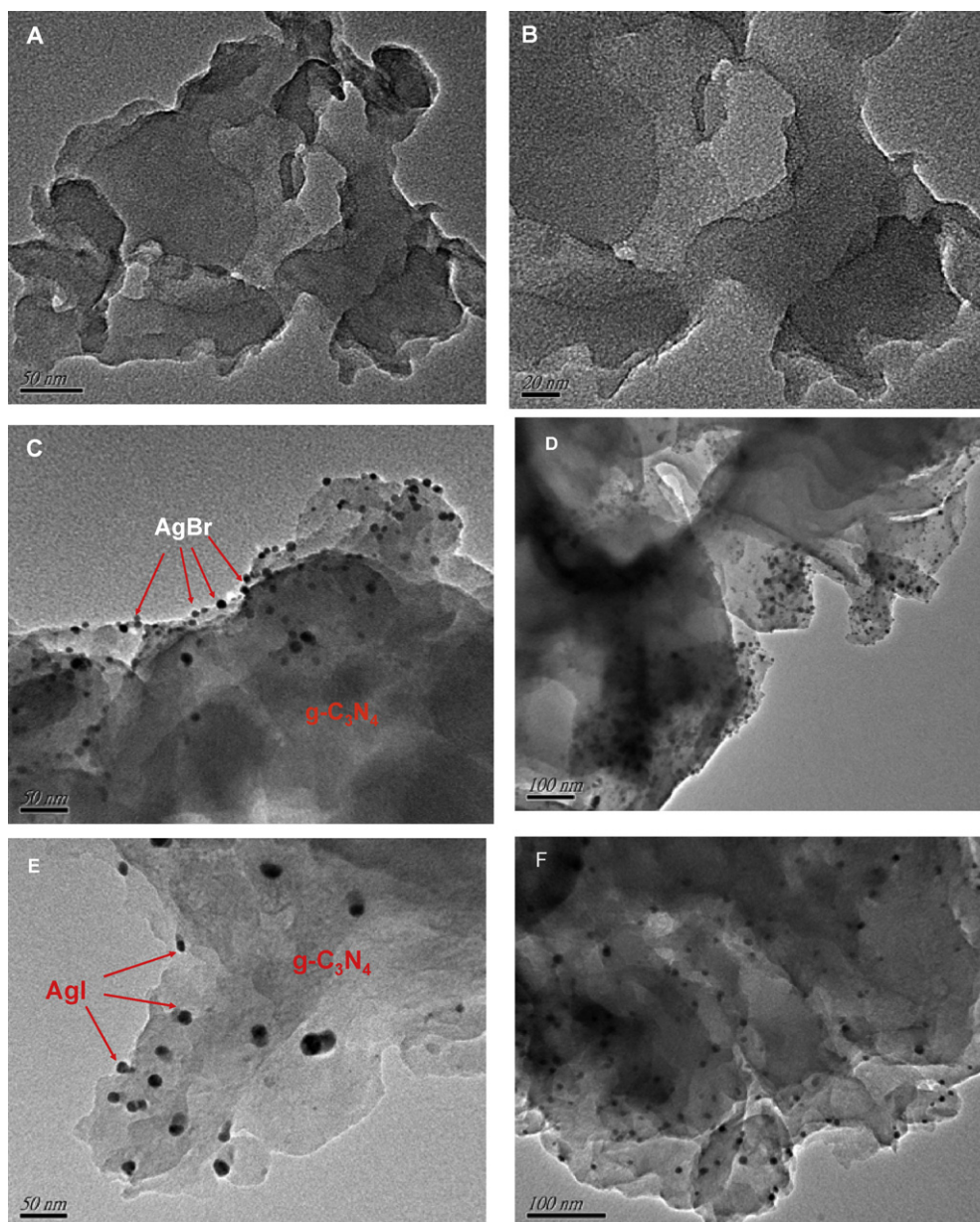


Fig. 6. TEM images of g-C₃N₄ (A and B), AgBr/g-C₃N₄ hybrid material (10%) (C), AgBr/g-C₃N₄ hybrid material (30%) (D), AgI/g-C₃N₄ composite (10%) (E) and AgI/g-C₃N₄ composite (30%) (F).

that the AgX/g-C₃N₄ composites had much lower recombination rate of photo-generated charge carriers. This demonstrated that the recombination of photogenerated charge carriers was greatly inhibited by the introduction of AgX, which showed the photogenerated electrons and holes in AgX/g-C₃N₄ hybrid materials had higher separation efficiency than those in the pure g-C₃N₄.

Generally speaking, photocatalytic reaction using semiconductors as catalysts involved the generation of electron and hole pairs. It was widely accepted that the separation efficiency of electrons and holes played a vital role in the photocatalytic reaction [73]: the higher the photocurrent was, the better the electron and hole separation efficiency would be, and thus the higher the photocatalytic activity would be [42,73]. To further understand the photogenerated charge separation and the electron transfer performance between g-C₃N₄ and AgX, the transient photocurrent responses of g-C₃N₄ and AgX/g-C₃N₄ hybrid material electrodes were recorded for several on-off cycles of visible light irradiation,

as shown in Fig. 11. g-C₃N₄ showed almost no photocurrent response. On the contrary, the AgX/g-C₃N₄ hybrid materials showed a noticeable photocurrent under visible light irradiation. It was also found that the AgX/g-C₃N₄ hybrid materials had the stable photocurrent, which indicated that the hybrid materials had lower rate to recombine electrons and holes [42,73]. This obvious increasing photocurrent also indicated less recombination and a more efficient separation of photogenerated electron and hole pairs for the AgX/g-C₃N₄ hybrid materials at the interface between AgX nanoparticles and g-C₃N₄. As can be seen from Fig. 11 (AgX/g-C₃N₄ sample), the photocurrent value rapidly decreased to zero as soon as the irradiation of light turns off, and the photocurrent came back to a constant value when the light was on again, which was reproducible. This result demonstrated that most photogenerated electrons were transferred to the back contact across the samples to produce photocurrent under visible light irradiation. The photocurrent of the AgBr/g-C₃N₄ and AgI/g-C₃N₄ hybrid material electrodes was found to increase by 21 and 8

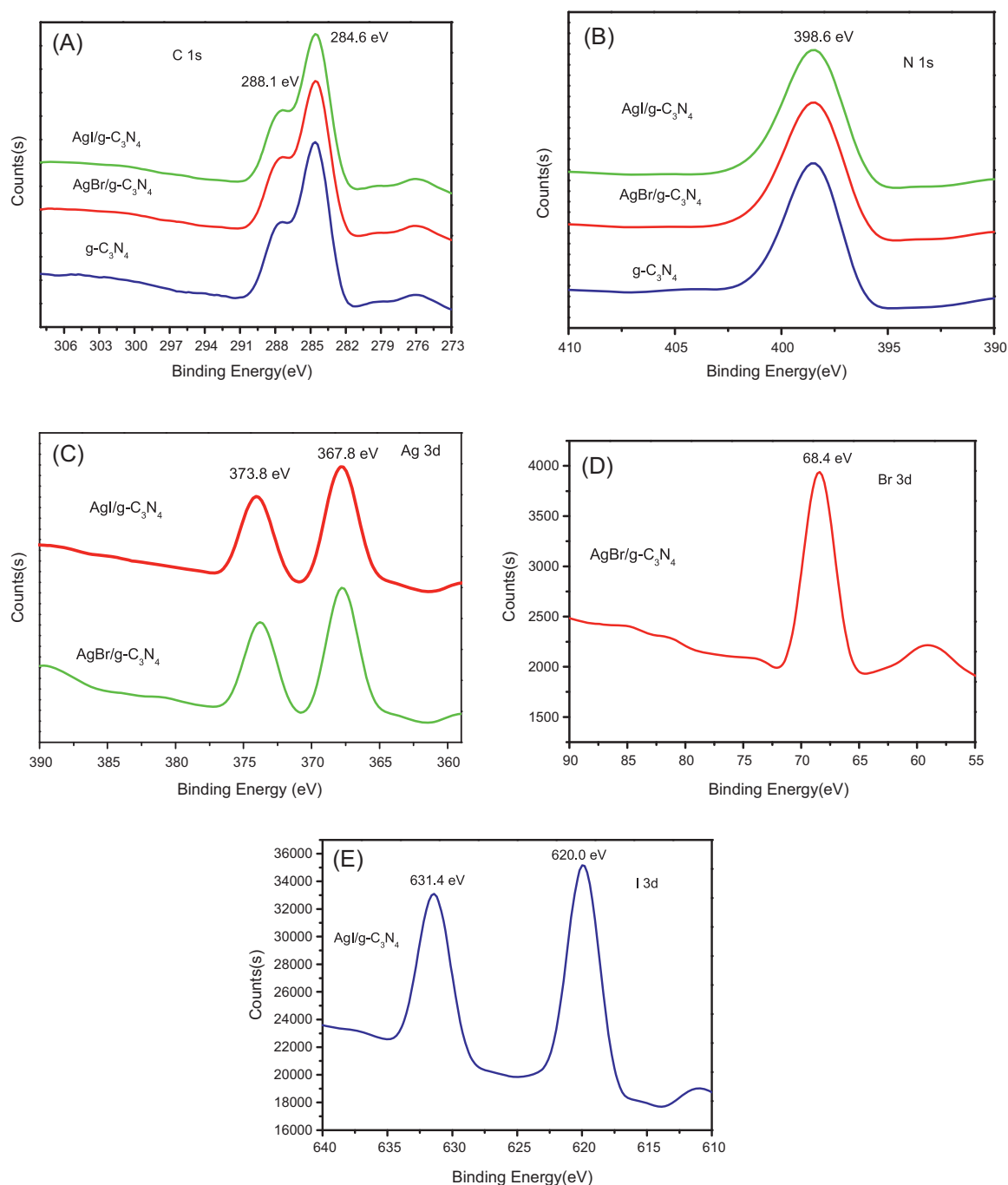


Fig. 7. XPS spectra of the samples: (A) C 1s and (B) N 1s of g-C₃N₄ and AgX/g-C₃N₄ hybrid materials, (C) Ag 3d of AgX/g-C₃N₄ hybrid materials, (D) Br 3d of AgBr/g-C₃N₄ hybrid material, and (E) I 3d of AgI/g-C₃N₄ composite.

times than that of the pure g-C₃N₄, respectively, which was in consistence with photocatalytic activity. The AgBr/g-C₃N₄ sample exhibited a higher photoelectric current than AgI/g-C₃N₄ hybrid material, while the pure g-C₃N₄ sample possessed the lowest photoelectric behavior, which was consistent with the order of their photocatalytic activity for MO dye degradation. As a result, the photocurrent enhancement of the AgI/g-C₃N₄ hybrid materials indicated the enhancing separation efficiency of photoinduced electrons and holes, which could be attributed to the synergetic effect of g-C₃N₄ and the AgX nanoparticles.

It was well known that the enhancement of photocatalytic performance of composite photocatalysts was mainly attributed to electron and hole transfer at the heterojunction interfaces [73]. When the AgX nanoparticles were introduced to g-C₃N₄, the two

types of semiconductor materials combined closely together and the heterojunction structure could be formed, which resulted in an effective photo-excited electron and hole separation in the two materials. The band gap of g-C₃N₄ was estimated as 2.7 eV according to the literatures [16] and the DRS analysis (Fig. 8). The band edge potential position of the g-C₃N₄ and AgI/g-C₃N₄ hybrid materials played an important role in studying the flowchart of photo-excited charge carriers. To give a direct analysis, the potentials of the conduction band (CB) and valence band (VB) edges of g-C₃N₄ and AgX were evaluated by Mulliken electronegativity theory

$$E_{CB} = X - E_c - \frac{1}{2}E_g$$

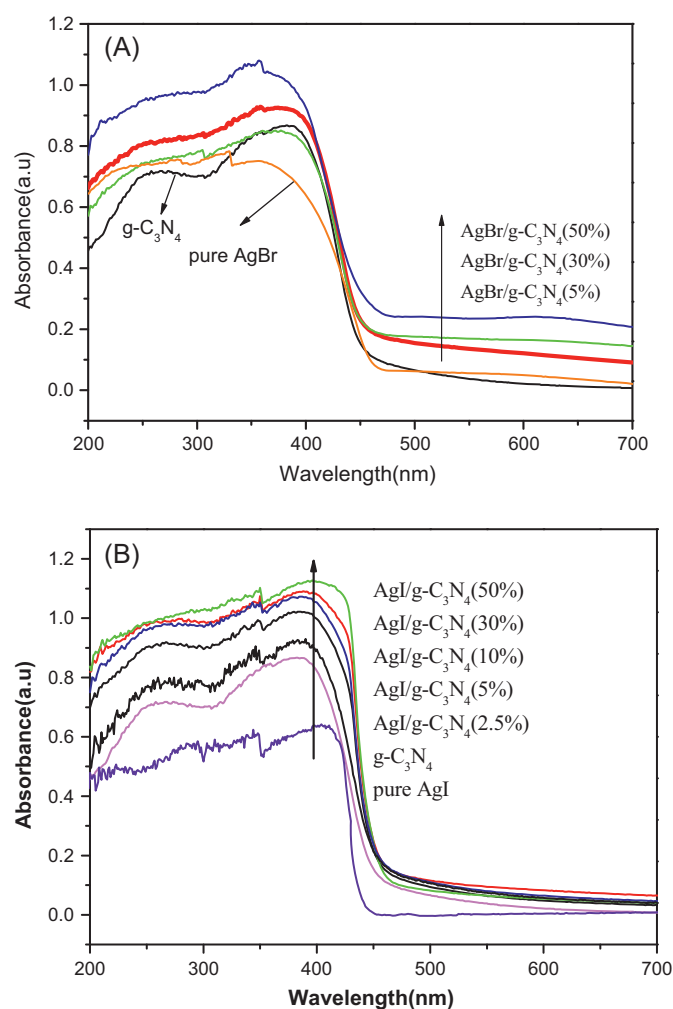


Fig. 8. UV-vis diffuse reflectance spectra of the samples: (A) AgBr/g-C₃N₄ hybrid materials and (B) AgI/g-C₃N₄ materials.

where X was the absolute electronegativity of the atom semiconductor, expressed as the geometric mean of the absolute electronegativity of the constituent atoms, and defined as the arithmetic mean of the atomic electro affinity and the first ionization energy; E_c was the energy of free electrons with the hydrogen scale (4.5 eV); E_g was the band gap of the semiconductor. Therefore, in the case of AgBr or AgI, the optical band gap was determined

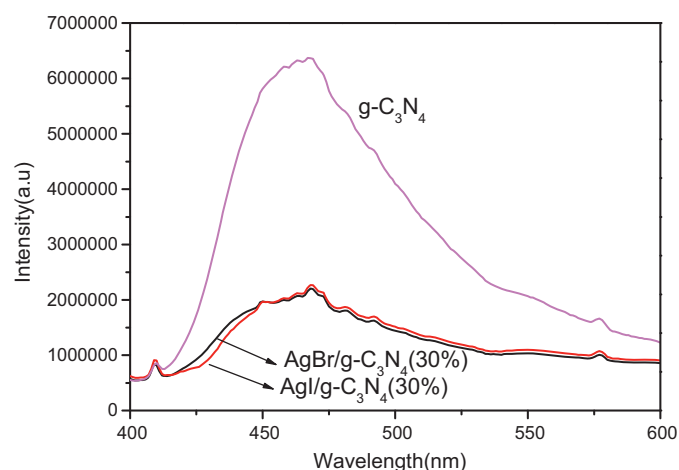


Fig. 10. PL spectra of g-C₃N₄, AgBr/g-C₃N₄ and AgI/g-C₃N₄ hybrid materials.

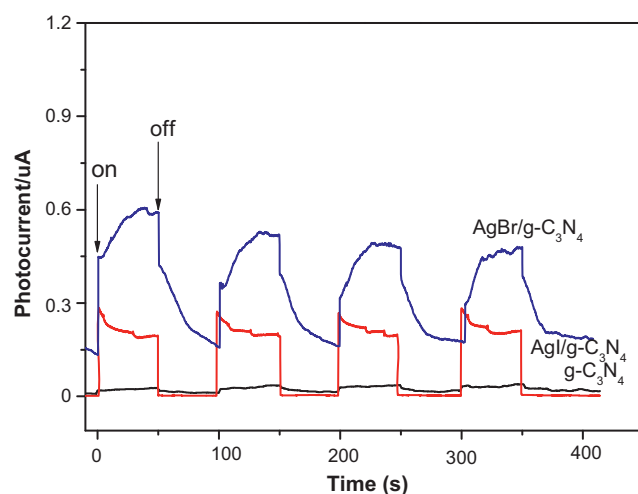


Fig. 11. Transient photocurrent responses of the pure g-C₃N₄, AgBr/g-C₃N₄ and AgI/g-C₃N₄ samples in 1 M Na₂SO₄ aqueous solution under visible light irradiation.

to be 2.6 eV and 2.8 eV, which was similar to the reported literatures [64]. Based on the band gap positions, the CB and VB edge potentials of g-C₃N₄ were determined at -1.13 eV and $+1.57$ eV, respectively [49]. The CB and VB edge potentials of AgBr were at 0 eV and $+2.6$ eV, respectively (conduction band of AgI: -0.42 eV, valence band of AgI: 2.38 eV). The CB and VB potentials of g-C₃N₄

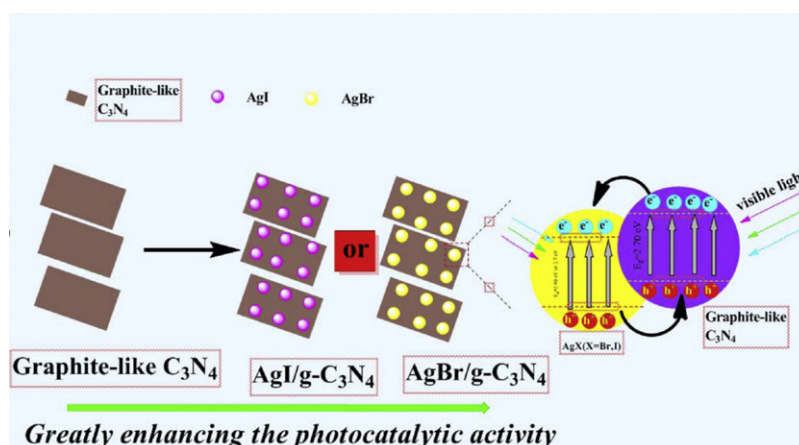


Fig. 9. Schematic illustration of AgX/g-C₃N₄ hybrid materials.

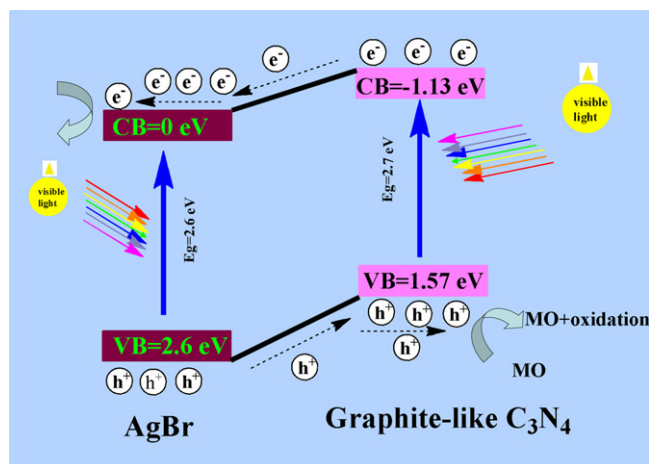


Fig. 12. The proposed charge separation process of AgBr/g-C₃N₄ heterostructures under visible light irradiation.

were more negative than those of AgBr and AgI. Therefore, when the hybrid material system was irradiated with visible light, the g-C₃N₄ and AgX nanoparticles in the composite photocatalyst both absorbed photons, as well as excited electron and hole pairs. The process could be described as follows: the electrons were promoted from the VB to the CB of the g-C₃N₄ and AgX nanoparticles, leaving the holes behind. The photogenerated electrons in the g-C₃N₄ layer structure could be easily transferred to the surface of the AgBr or AgI nanoparticles, and the holes generated in the VB of AgBr or AgI nanoparticles could migrate to the surface of g-C₃N₄, which promoted the effective separation of photoexcited electron–hole pairs and decreased the probability of electron and hole recombination. Consequently, the small AgX nanoparticles deposited on the surface of the g-C₃N₄ could form the heterojunction structure, which was beneficial to the increase of the photocatalytic activity. The enhancement of photocatalytic activity due to the heterojunction structure could also be shown in other systems, such as ZnO/BiOI [73] and C₃N₄/Bi₂WO₆ [49]. The proposed charge separation process of AgX/g-C₃N₄ heterostructures under visible light irradiation is shown in Figs. 12 and S7.

4. Conclusion

Novel visible-light-driven AgX/g-C₃N₄ hybrid materials were synthesized by introducing AgX nanoparticles with the facile water bath method. AgX nanoparticles were evenly distributed on the surface of g-C₃N₄ and the heterostructures were formed. The as-prepared AgX/g-C₃N₄ hybrid materials displayed an enhancement of photocatalytic activity, which was greatly improved in comparison with the pure g-C₃N₄ as well as AgX nanoparticles. After introduction of AgX nanoparticles, the photocurrent of the sample was enhanced significantly under visible light irradiation. The increase of photocatalytic activity of the AgX/g-C₃N₄ hybrid materials was attributed to the synergic effect between g-C₃N₄ and AgX, including optical property, better dispersion and small size. The heterostructures between AgX and g-C₃N₄ were beneficial for the transfer of photogenerated electrons and holes, thereby the photocatalytic efficiency was improved dramatically. In a word, the high photocatalytic activity of the hybrid materials could be attributed to the strong coupling between g-C₃N₄ and AgX, which facilitated interfacial charge transfer and inhibited electron–hole recombination.

Acknowledgments

The authors genuinely appreciate the financial support of this work from the National Nature Science Foundation of China (No. 21007021, 21177050, 21076099 and 21206060), Society Development Fund of Zhenjiang (SH2011011 and SH2012020).

Appendix A. Supplementary data

Supplementary data associated with this article can be found, in the online version, at <http://dx.doi.org/10.1016/j.apcatb.2012.08.015>.

References

- [1] X. Han, Q. Kuang, M. Jin, Z. Xie, L. Zheng, *Journal of the American Chemical Society* 131 (2009) 3152–3153.
- [2] A. McLaren, T. Valdes-Solis, G.Q. Li, S.C. Tsang, *Journal of the American Chemical Society* 131 (2009) 12540–12541.
- [3] S.H. Baek, K.S. Choi, T.F. Jaramillo, G.D. Stucky, E.W. McFarland, *Advanced Materials* 15 (2003) 1269–1273.
- [4] A. Kubacka, M. Fernandez-García, G. Colon, *Chemical Reviews* 112 (2012) 1555–1614.
- [5] L.L. Zhang, Z. Xiong, X.S. Zhao, *ACS Nano* 4 (2010) 7030–7036.
- [6] X. Chen, S. Shen, L. Guo, S.S. Mao, *Chemical Reviews* 110 (2010) 6503–6570.
- [7] H. Gao, C. Liu, H.E. Jeong, P. Yang, *ACS Nano* 6 (2012) 234–240.
- [8] Q. Xiang, J. Yu, M. Jaroniec, *Chemical Society Reviews* 41 (2012) 782–796.
- [9] X. An, J.C. Yu, *RSC Advances* 1 (2011) 1426–1434.
- [10] P. Li, Z. Wei, T. Wu, Q. Peng, Y. Li, *Journal of the American Chemical Society* 133 (2011) 5660–5663.
- [11] X. Zhang, Z.H. Ai, F.L. Jia, L.Z. Zhang, *Journal of Physical Chemistry C* 112 (2008) 747–753.
- [12] J. Xia, S. Yin, H. Li, H. Xu, Y. Yan, Q. Zhang, *Langmuir* 27 (2011) 1200–1206.
- [13] J. Xia, S. Yin, H. Li, H. Xu, L. Xu, Y. Xu, *Dalton Transactions* 40 (2011) 5249–5258.
- [14] S.S. Dunkle, R.J. Helmich, K.S. Suslick, *Journal of Physical Chemistry C* 113 (2009) 11980–11983.
- [15] X. Chen, L. Liu, P.Y. Yu, S.S. Mao, *Science* 331 (2011) 746–750.
- [16] X. Wang, K. Maeda, A. Thomas, K. Takanabe, G. Xin, J.M. Carlsson, K. Domen, M. Antonietti, *Nature Materials* 8 (2009) 76–80.
- [17] K. Maeda, X. Wang, Y. Nishihara, D. Lu, M. Antonietti, K. Domen, *Journal of Physical Chemistry C* 113 (2009) 4940–4947.
- [18] S.C. Yan, Z.S. Li, Z.G. Zou, *Langmuir* 25 (2009) 10397–10401.
- [19] Y. Wang, X. Wang, M. Antonietti, *Angewandte Chemie International Edition* 51 (2012) 68–89.
- [20] F. Su, S.C. Mathew, L. Möhlmann, M. Antonietti, X. Wang, S. Blechert, *Angewandte Chemie International Edition* 50 (2011) 657–660.
- [21] Y. Guo, S. Chu, S. Yan, Y. Wang, Z. Zou, *Chemical Communications* 46 (2010) 7325–7327.
- [22] F. Su, S.C. Mathew, G. Lipner, X. Fu, M. Antonietti, S. Blechert, X. Wang, *Journal of the American Chemical Society* 132 (2010) 16299–16301.
- [23] F. Goettmann, A. Fischer, M. Antonietti, A. Thomas, *Angewandte Chemie International Edition* 45 (2006) 4467–4471.
- [24] X. Chen, Y.S. Jun, K. Takanabe, K. Maeda, K. Domen, X. Fu, M. Antonietti, X. Wang, *Chemistry of Materials* 21 (2009) 4093–4095.
- [25] X.H. Li, J. Zhang, X. Chen, A. Fischer, A. Thomas, M. Antonietti, X. Wang, *Chemistry of Materials* 23 (2011) 4344–4348.
- [26] Y. Wang, X. Wang, M. Antonietti, Y. Zhang, *ChemSusChem* 3 (2010) 435–439.
- [27] G. Dong, L. Zhang, *Journal of Materials Chemistry* 22 (2012) 1160–1166.
- [28] Y. Cui, J. Zhang, G. Zhang, J. Huang, P. Liu, M. Antonietti, X. Wang, *Journal of Materials Chemistry* 21 (2011) 13032–13039.
- [29] K. Kailasam, J.D. Epping, A. Thomas, S. Losse, H. Junge, *Energy & Environmental Science* 4 (2011) 4668–4674.
- [30] X. Chen, J. Zhang, X. Fu, M. Antonietti, X. Wang, *Journal of the American Chemical Society* 131 (2009) 11658–11659.
- [31] X. Wang, X. Chen, A. Thomas, X. Fu, M. Antonietti, *Advanced Materials* 21 (2009) 1609–1612.
- [32] Z. Ding, X. Chen, M. Antonietti, X. Wang, *ChemSusChem* 4 (2011) 274–281.
- [33] J. Zhang, M. Grzelczak, Y. Hou, K. Maeda, K. Domen, X. Fu, M. Antonietti, X. Wang, *Chemical Science* 3 (2012) 443–446.
- [34] L. Ge, C. Han, J. Liu, Y. Li, *Applied Catalysis A* 409–410 (2011) 215–222.
- [35] Y. Wang, J. Yao, H. Li, D. Su, M. Antonietti, *Journal of the American Chemical Society* 133 (2011) 2362–2365.
- [36] Y. Zhang, T. Mori, J. Ye, M. Antonietti, *Journal of the American Chemical Society* 132 (2010) 6294–6295.
- [37] Y. Wang, Y. Di, M. Antonietti, H. Li, X. Chen, X. Wang, *Chemistry of Materials* 22 (2010) 5119–5121.
- [38] G. Liu, P. Niu, C. Sun, S.C. Smith, Z. Chen, G.Q. Lu, H.M. Cheng, *Journal of the American Chemical Society* 132 (2010) 11642–11648.
- [39] J. Zhang, J. Sun, K. Maeda, K. Domen, P. Liu, M. Antonietti, X. Fu, X. Wang, *Energy & Environmental Science* 4 (2011) 675–678.
- [40] S.C. Yan, Z.S. Li, Z.G. Zou, *Langmuir* 26 (2010) 3894–3901.

- [41] Y. Wang, J. Zhang, X. Wang, M. Antonietti, H. Li, *Angewandte Chemie International Edition* 49 (2010) 3356–3359.
- [42] Q. Xiang, J. Yu, M. Jaroniec, *Journal of Physical Chemistry C* 115 (2011) 7355–7363.
- [43] Y. Zhang, T. Mori, L. Niu, J. Ye, *Energy & Environmental Science* 4 (2011) 4517–4521.
- [44] X.H. Li, J.S. Chen, X. Wang, J. Sun, M. Antonietti, *Journal of the American Chemical Society* 133 (2011) 8074–8077.
- [45] C.G. Silva, J.L. Faria, *ChemSusChem* 3 (2010) 609–618.
- [46] H. Yan, H. Yang, *Journal of Alloys and Compounds* 509 (2011) L26–L29.
- [47] S.C. Yan, S.B. Lv, Z.S. Li, Z.G. Zou, *Dalton Transactions* 39 (2010) 1488–1491.
- [48] K. Takanabe, K. Kamata, X. Wang, M. Antonietti, J. Kubota, K. Domen, *Physical Chemistry Chemical Physics* 12 (2010) 13020–13025.
- [49] L. Ge, C. Han, J. Liu, *Applied Catalysis B* 108–109 (2011) 100–107.
- [50] Y. Wang, R. Shi, J. Lin, Y. Zhu, *Energy & Environmental Science* 4 (2011) 2922–2929.
- [51] X. Xu, G. Liu, C. Random, J.T.S. Irvine, *International Journal of Hydrogen Energy* 36 (2011) 13501–13507.
- [52] H. Pan, X. Li, Z. Zhuang, C. Zhang, *Journal of Molecular Catalysis A: Chemical* 345 (2011) 90–95.
- [53] J.W. Lee, H.J. Jeon, H.J. Shin, J.K. Kang, *Chemical Communications* 48 (2012) 422–424.
- [54] H. Wang, J. Gao, T. Guo, R. Wang, L. Guo, Y. Liu, J. Li, *Chemical Communications* 48 (2012) 275–277.
- [55] Z. Lou, B. Huang, X. Qin, X. Zhang, Z. Wang, Z. Zheng, H. Cheng, P. Wang, Y. Dai, *Catalysis Today* 175 (2011) 256–263.
- [56] L. Liu, H. Xu, H. Li, Y. Xu, J. Xia, S. Yin, *Journal of Physics and Chemistry of Solids* 73 (2012) 523–529.
- [57] Y. Li, H. Zhang, Z. Guo, J. Han, X. Zhao, Q. Zhao, S.J. Kim, *Langmuir* 24 (2008) 8351–8357.
- [58] C. Hu, X. Hu, L. Wang, J. Qu, A. Wa, *Environmental Science and Technology* 40 (2006) 7903–7907.
- [59] D. Wu, M. Long, *Surface and Coatings Technology* 206 (2011) 1175–1179.
- [60] M.A. Asia, C. He, M. Su, D. Xia, L. Lin, H. Deng, Y. Xiong, R. Qiu, X. Li, *Catalysis Today* 175 (2011) 256–263.
- [61] B. Krishnakumar, B. Subash, M. Swaminathan, *Separation and Purification Technology* 85 (2012) 35–44.
- [62] C. Wu, L. Shen, Y.C. Zhang, Q. Huang, *Materials Letters* 66 (2012) 83–85.
- [63] J. Cao, B. Luo, H. Lin, S. Chen, *Journal of Hazardous Materials* 190 (2011) 700–706.
- [64] Y. Bi, S. Ouyang, J. Cao, J. Ye, *Physical Chemistry Chemical Physics* 13 (2011) 10071–10075.
- [65] H. Xu, Y. Xu, H. Li, J. Xia, J. Xiong, S. Yin, C. Huang, H. Wan, *Dalton Transactions* 41 (2012) 3387–3394.
- [66] G. Li, K.H. Wong, X. Zhang, C. Hu, J.C. Yu, R.C.Y. Chang, P.K. Wong, *Chemosphere* 76 (2009) 1185–1191.
- [67] J.F. Guo, B. Ma, A. Yin, K. Fan, W.L. Dai, *Applied Catalysis B* 101 (2011) 580–586.
- [68] J. Cao, B. Luo, H. Lin, S. Chen, *Journal of Molecular Catalysis A: Chemical* 344 (2011) 138–144.
- [69] S. Rodrigues, S. Uma, I.N. Martyanov, K.J. Klabunde, *Journal of Catalysis* 233 (2005) 405–410.
- [70] A. Pourahmad, S. Sohrabnezhad, E. Kashefian, *Spectrochimica Acta, Part A* 77 (2010) 1108–1114.
- [71] Y. Zang, R. Farnood, J. Currie, *Chemical Engineering Science* 64 (2009) 2881–2886.
- [72] L.X. Yang, S.L. Luo, Y. Li, Y. Xiao, Q. Kang, Q.Y. Cai, *Environmental Science and Technology* 44 (2010) 7641–7646.
- [73] J. Jiang, X. Zhang, P.B. Sun, L.Z. Zhang, *Journal of Physical Chemistry C* 115 (2011) 20555–20564.
- [74] Y. Wang, J. Mo, W. Cai, L. Yao, L. Zhang, *Materials Letters* 56 (2002) 502–506.
- [75] Y. Zhang, Z.R. Tang, X. Fu, Y.J. Xu, *Applied Catalysis B* 106 (2011) 445–452.
- [76] P. Wang, B. Huang, Q. Zhang, X. Zhang, X. Qin, Y. Dai, J. Zhan, J. Yu, H. Liu, Z. Lou, *Chemistry—A European Journal* 16 (2010) 10042–10047.
- [77] V. Subramanian, E.E. Wolf, P.V. Kamat, *Journal of the American Chemical Society* 126 (2004) 4943–4950.
- [78] Y. Zheng, C. Chen, Y. Zhan, X. Lin, Q. Zheng, K. Wei, J. Zhu, *Journal of Physical Chemistry C* 112 (2008) 10773–10777.
- [79] J. Lu, I. Do, L.T. Drzal, R.M. Worden, I. Lee, *ACS Nano* 2 (2008) 1825–1832.
- [80] M. Murdoch, G.I.N. Waterhouse, M.A. Nadeem, J.B. Metson, M.A. Keane, R.F. Howe, J. Liorca, H. Idriss, *Nature Chemistry* 3 (2011) 489–492.
- [81] L. Ge, C. Han, *Applied Catalysis B* 117–118 (2012) 268–274.